Journal of Environmental Chemical Engineering 13 (2025) 116948

Contents lists available at ScienceDirect

Journal of Environmental Chemical Engineering

journal homepage: www.elsevier.com/locate/jece

MOF-derived Ni-Co bimetallic catalyst facilitated the gasification of surface carbon during DRM process

Hongchuan Liu [a,c], Meirong Dong [a,c,*], Junchang Xiong [a,c], Zehua Huang [a,c], Huaming Hou [b,**], Youcai Liang [a,c], Jidong Lu [a,c]

[a] School of Electric Power Engineering, South China University of Technology, Guangzhou, Guangdong 510640, China
[b] National Energy Center for Coal to Clean Fuels, Synfuels China Technology Co., Ltd., Beijing 101407, China
[c] Guangdong Province Engineering Research Center of High Efficient and Low Pollution Energy Conversion, Guangzhou, Guangdong 510640, China

ARTICLE INFO

Keywords:
Metal-organic frameworks
Dry reforming of methane
Metal-support interaction
Carbon deposition

ABSTRACT

In order to improve the reactivity of dry reforming of methane, the MOF-derived bimetallic catalyst Ni-Co/CeO_2-M was constructed using Ce-UiO-66 as the precursor. CeO_2 lattice constant shift provided evidence for the formation of Ni-O-Ce solid solution, and metal nanoparticles encapsulated by the thin layer of support oxide were observed in the ultrastructure. These strong metal-support interactions effectively enhanced the dispersion and stability of active metals. Meanwhile, more charge transfer between Ni-Co promoted reactant activation and intermediate conversion, which played positive roles in avoiding oxygen species oversorption and catalyst peroxidation. Thus, a synergistic mechanism of surface interspecies reactions and oxygen vacancy cycling supported by efficient oxygen mobility was established. DRM tests showed that CO_2 conversion and CO yield of the MOF-derived materials did not decline during the period examined. Particularly noteworthy was the favorable surface carbon gasification kinetics of Ni-Co/CeO_2-M, which contributed to the enhancement of reactivity and suppression of inactive carbon accumulation. This work provides new perspectives on the interfacial property modulation and anti-coking strategies for DRM catalysts.

1. Introduction

Carbon emission reduction and sustainable development are common pursuits, and efforts in Carbon Capture, Utilization and Storage (CCUS) and energy high-value conversion have been increasing [1–3]. Dry reforming of methane (DRM) is a catalytic reaction between CH_4 and CO_2 to produce H_2 and CO, offering an efficient method for both highly valuable utilization of CH_4 and recovery of CO_2 resources [2,4,5]. Due to the catalyst deactivation issue resulted from sintering and coking at high temperatures, the reactivity and stability of DRM still need to be improved, and the design of high-performance catalytic materials is the key [2,4,6]. Base metal catalysts represented by Ni have the advantage of low cost and good catalytic activity, but severe carbon deposition remains a major challenge [4,5,7–9]. Bimetallic catalysts can provide a couple-gain effect in DRM with the help of different active metal characteristics and intermetallic interactions, and are considered to be an effective solution for controlling carbon accumulation.

The introduction of second elements such as Ag [10], Pt [11], Cr [12], Ta [12], Cu [13], Fe [7] into the Ni-based catalyst to construct a bimetallic system can optimize the catalytic activity and stability of metal nanoparticles (MNPs). In addition, Co has similar electronic structure with Ni, which is prone to form intermetallic interactions and proved to be a good choice for the construction of economical and efficient bimetallic catalyst systems [14–16]. Wang et al. [8] and Zou et al. [15] prepared Ni-Co bimetallic catalysts using different synthetic methods, respectively, and both confirmed that Ni-Co alloys modified by special structures played key roles in enhancing DRM reactivity and inhibiting carbon deposition. Ou et al. [17] suggested that the favored performance of Ni-Co alloys for DRM reaction could originate from the surface charge transfer induced by Co segregation, which caused a reduction in CO_2 activation energy barrier and the accelerated consumption of carbon-containing species. In addition to inducing the interaction between active metals, the effect of Co doping on the support components has also attracted attention. Yang et al. [6] loaded compositionally controllable Ni@Co core-shell structured bimetallic alloys onto CeO_2, and found that the Co shells not only influenced the

* Corresponding author at: School of Electric Power Engineering, South China University of Technology, Guangzhou, Guangdong 510640, China.
** Corresponding author.
E-mail addresses: epdongmr@scut.edu.cn (M. Dong), houhuaming@synfuelschina.com.cn (H. Hou).

https://doi.org/10.1016/j.jece.2025.116948
Received 29 January 2025; Received in revised form 8 April 2025; Accepted 4 May 2025
Available online 5 May 2025

metal-support interaction (MSI), but also synergistically improved the adsorption of CO_2 and the elimination of carbon species with CeO_2 support. Therefore, by modulating the Ni-Co bimetallic structure and catalytic interface, the intermetallic interaction and MSI can be optimized while increasing the utilization efficiency of the active metal atoms, so as to enhance the comprehensive catalytic performance [6, 15]. However, it is difficult to realize the improvement of active site assignment and the modulation of interfacial properties of bimetallic catalysts via conventional preparation methods, while the existing overly complicated strategies are often unfavorable for replication. Thus, it is necessary to further develop facile modulation approaches for bimetallic catalysts.

Metal organic frameworks (MOFs), as ordered porous materials, offer several advantages including high specific surface area and topological tunability, making them highly attractive for gas storage and separation [18]. However, the limited thermal stability makes the structure of MOFs susceptible to damage at high temperatures. Derivatives obtained from MOFs as precursors can inherit the morphological structure while extending the stability and conductivity [19], which have found successful applications in environmental, energy storage and catalysis [20–22]. Over the past few years, MOF-derived materials have also been increasingly used in DRM reaction. For example, Komarala et al. [23] found that good reactant conversions could be achieved in DRM by ultrasonically coalescing Ni- and La-MOF followed by calcination at different temperatures. Tu et al. [24] reported a MOF-derived carbide catalyst, which was obtained by incorporating Ni into Ce-MOF-808 via post-synthetic modification method. The results confirmed that well-dispersed metal ions in the MOF matrix could effectively inhibit the agglomeration of MNPs. Moreover, Alli et al. [25, 26] examined the synthesis processes of MOF-derived NiCe-based catalysts, including Ni loading, organic ligands, and thermal treatment conditions, these works provide the reference for the development and application of MOF-derived materials in DRM. In our previous study [27], we revealed that Ce-MOFs with different topologies could be used as precursors to modulate the support morphology, as the improved catalysts obtained significantly better textural properties and CO_2 adsorption activation capacity. Although the large surface area and structural diversity of MOFs have been proven to modify DRM catalysts, Ni-based monometallic catalysts still face challenges in anti-coking and long-term stability. Therefore, the potential of MOFs in the modification of bimetallic catalysts needs to be further explored, and it is expected to be a favorable approach for the fine construction of catalyst systems.

In this work, the MOF precursor is intended to offer a two-fold boost. First, its ordered porous structure and large deposition surface lay the foundation for highly dispersed and homogeneous distribution of active metals, which enhances the atom utilization efficiency and the amount of active sites. Second, the controlled pyrolysis process of the MOF precursor plays a key role in inducing metal-support structural reorganization and metal-particle rearrangement, which make it possible to modulate the MSI and bimetallic synergism. Based on the above ideas, a MOF-derived bimetallic catalyst, Ni-Co/CeO_2-M, was synthesized by in-situ impregnation with Ce-UiO-66 to investigate the effectiveness of MOF materials in bimetallic site modulation and catalytic interface optimization. DRM performance, including initial catalytic activity, stability and carbon deposition behavior, was comprehensively evaluated by comparison with MOF-derived Ni monometallic catalyst and conventionally supported catalysts. In addition, various characterizations were adopted to elucidate the structure-activity relationships, thus providing a valuable reference for the construction of high-performance DRM catalysts.

2. Experimental section

2.1. Catalyst synthesis

The MOF precursor, Ce-UiO-66, was synthesized following a previous report [28]. Specifically, a solution of 3.717 g of terephthalic acid (1,4-H_2BDC) in 84 mL of dimethylformamide (DMF) was prepared in a glass bottle. To this, 42 mL of $(NH_4)_2Ce(NO_3)_6$ aqueous solution (0.533 mol/L) was dropped slowly. The mixture was then sealed and reacted at 100 °C for 15 minutes. Having cooled down, the precipitate was collected by centrifugation and washed thoroughly with DMF, and followed by solvent exchange with acetone. Subsequently, the solid was dried at 70 °C for about 15 h to yield activated Ce-UiO-66 MOF.

Ni and Co were introduced into the activated Ce-UiO-66 via the impregnation method. The required amounts of $Ni(NO_3)_2•6H_2O$ and $Co(NO_3)_2•6H_2O$ were fully dissolved in deionized water according to the specified metal loading (10 wt% Ni + 5 wt% Co). To the solution added Ce-UiO-66 powder matching the metal loading (mass loss due to heat treatment needed to be taken into account, see Section 3.1). The suspension was stirred thoroughly at room temperature overnight and then drained at 105 °C for 15 h. A stepwise controlled pyrolysis procedure was employed to avoid structural collapse due to rapid heating. The dried solid was first heated from room temperature to 460 °C at 3 °C/min and held for 3 h, then to 600 °C at 10 °C/min and held for 6 h. The final MOF-derived bimetallic catalyst obtained was denoted as Ni-Co/CeO_2-M. The MOF-derived monometallic catalyst Ni/CeO_2-M was prepared using the same process described above at a Ni metal loading of 10 wt%.

In addition, conventionally supported mono- and bimetallic catalysts were prepared as control samples using a typical impregnation process. A monometallic solution was obtained by dissolving 0.826 g of $Ni(NO_3)_2•6H_2O$ in 20 mL of deionized water, and a bimetallic solution was obtained by dissolving 0.874 g of $Ni(NO_3)_2•6H_2O$ and 0.436 g of $Co(NO_3)_2•6H_2O$ in 20 mL of deionized water. To each of the above two solutions was added 1.5 g of CeO_2 support powder, which was obtained by calcining $Ce(NO_3)_3•6H_2O$ at 600 °C for 6 h in a muffle furnace. The suspensions were stirred overnight and dried completely at 105 °C. The dried solids were subsequently calcined at 10 °C/min up to 600 °C for 6 h, and the resulting conventional mono- and bimetallic catalysts were named Ni-CeO_2-C and Ni-Co/CeO_2-C, respectively.

2.2. Characterization method

Inductively coupled plasma optical emission spectrometry (ICP-OES) was performed using a PerkinElmer Optima 8300 instrument to determine the metal loading of catalysts. Approximately 20 mg of solid powder sample was completely dissolved by acid digestion method and diluted to a constant volume, then evaporated and excited by the plasma heat source. The concentration of different elements was determined by atomic emission spectroscopy, and the actual metal content in the sample was calculated according to the conversion formula Weight% $= (C_{ICP}\times V_{sol}\times M)/m_{sample}$. Among them, C_{ICP} is the element concentration measured by ICP-OES, V_{sol} is the volume of digestion solution, M is the dilution multiple, and m_{sample} is the sample quality. N_2 adsorption-desorption was conducted on a Quantachrome Autosorb iQ system. Prior to the testing, degassing at 200 °C for 6 h was required to ensure reliable results. High-resolution transmission electron microscopy (HRTEM) photographs were obtained by a JEM-F200 (Cyro) microscope. High-angle annular dark-field scanning transmission electron microscopy (HAADF-STEM) images and energy-dispersive spectrometer (EDS) elemental mapping were acquired by a FEI Talos F200 microscope at a working voltage of 200 kV. The samples were ultrasonically dispersed in ethanol solvent and dried on carbon-coated copper grids prior to photographing.

X-ray powder diffraction (XRD) patterns were recorded using a PANalytical X'Pert Powder diffractometer at a sweep rate of 6 °/min. The crystal size was determined using Scherrer's formula, $D = K\lambda/(\beta\cos\theta)$, where K denotes Scherrer's constant, λ represents the wavelength of the X-ray, and β and θ are the full-width at half maximum (FWHM) and the diffraction angle of the corresponding peaks, respectively. The CeO_2 lattice constant a was calculated based on cubic lattice

formula $d^2=a^2/(h^2+k^2+l^2)$, where d is the lattice spacing, and h, k, and l are the Miller indices of the lattice. X-ray photoelectron spectroscopy (XPS) data were acquired with a Kratos Axis Supra+ instrument, and the deconvolution was performed using the Voigt profile function after charge calibration to C 1 s at 284.8 eV.

Temperature programmed tests were conducted using a Micromeritics AutoChem II 2920 chemisorber and degassed prior to testing. H_2 temperature programmed reduction (H_2-TPR) was accomplished with a heating rate of 10 °C/min in a 10 vol% H_2/Ar gas flow at 20 mL/min. While CO_2 temperature-programmed desorption (CO_2-TPD) was first adsorbed CO_2 to saturation and then desorbed in an Ar stream. Raman and Fourier transform infrared (FTIR) data were collected by a HJY LabRAM Aramis system and a Bruker VERTEX 70 infrared spectrometer, respectively. Thermogravimetric analysis (TGA) was undertaken using a Netzsch STA 449F1 Jupiter apparatus. Approximately 10 mg of spent catalyst was heated to 800 °C in a 30 mL/min Air at 10 °C/min, and the dTG curve was the derivative of the TG curve.

2.3. Catalytic assessment

DRM performance was tested in a compact tube furnace at ambient pressure. Internal and external mass diffusion effects were excluded through pre-experiments before evaluating catalytic performance. 100 mg of catalyst powder was uniformly loaded into a quartz boat and placed in a tube furnace. Prior to the methane reforming reaction, pre-activation was conducted with a 30 mL/min reducing mixture of 20 vol% H_2/N_2 at 800 °C for 1 h. Upon completion of the pre-activation, the temperature was adjusted to the preset value in a N_2 stream. Afterwards, DRM reaction was performed by switching to a feedstock mixture of CH_4:CO_2:N_2 = 1:1:3 at 60 mL/min. The product components were checked by gas chromatography (GC), and the conversion of reactants (X_i) and yield of products (Y_i) were calculated as follows:

$$X_i = \frac{F_{i,\mathrm{in}} - F_{i,\mathrm{out}}}{F_{i,\mathrm{in}}} \times 100\% \tag{1}$$

$$Y_{\mathrm{CO}} = \frac{F_{\mathrm{CO,out}}}{F_{\mathrm{CH_4,in}} + F_{\mathrm{CO_2,in}}} \times 100\% \tag{2}$$

$$Y_{\mathrm{H_2}} = \frac{F_{\mathrm{H_2,out}}}{2 \times F_{\mathrm{CH_4,in}}} \times 100\% \tag{3}$$

The H_2/CO molar ratio of the product was defined as:

$$\mathrm{H_2}\Big/\mathrm{CO} = \frac{F_{\mathrm{H_2,out}}}{F_{\mathrm{CO,out}}} \tag{4}$$

where F_i means the flow rate, in mol/min; the sub-labels "in" and "out" refer to the inflow and outflow gas, respectively. The initial activity was obtained by 0.5 h DRM at different temperatures, and the stability test was performed at 700 ℃.

2.4. Kinetic analysis of surface carbon gasification

In DRM reaction, CO_2 is the sole oxygen source to oxidize the carbon species on catalyst surface, and the overall reaction can be described as a reverse-Boudouard reaction (Eq. (5)). Therefore, to probe the elimination behavior of the surface carbon species in an approximation of the actual reaction environment, the post-reaction catalyst (~10 mg) was heated in a pure CO_2 stream. A modified Wigner-Polanyi kinetic equation (Eq. (6)) was used to describe the carbon gasification process [3]. Obviously, the partial pressure of CO_2 gas $p_{CO2} = 1$ in this case. Noting that the reaction order $n = 1$ for the surface carbon concentration θ^* has been confirmed [29], Eq. (6) can be rewritten as Eq. (7) incorporating the ramping rate β. Denote T_M as the horizontal coordinate temperature of the peak of the dTG curve, so the derivative with respect to temperature is 0 at T_M, which gives Eq. (8). Eventually, Eq. (9) can be obtained after equation deformation, which is used to fit and calculate kinetic parameters.

$$C^* + CO_2 = 2CO + {}^* \tag{5}$$

$$r = -\frac{\mathrm{d}\theta^*}{\mathrm{d}t} = A p_{\mathrm{CO_2}}^m [\theta^*]^n \exp\left[-\frac{E_a}{RT}\right] \tag{6}$$

$$-\frac{\mathrm{d}\theta^*}{\mathrm{d}T}\beta = A\theta^* \exp\left[-\frac{E_a}{RT}\right] \tag{7}$$

$$\frac{\mathrm{d}}{\mathrm{d}T}\left[\theta^* \frac{A}{\beta} \exp\left(\frac{E_a}{RT}\right)\right]_{T_M} = 0 \tag{8}$$

$$\ln\left(\frac{T_M^2}{\beta}\right) = \frac{E_a}{RT_M} + \ln\left(\frac{E_a}{AR}\right) \tag{9}$$

Among them, r is the carbon gasification rate, θ^* is the surface carbon concentration, t represents the time, A denotes the preexponential factor, p_{CO2} refers to the CO_2 partial pressure, m and n are reaction orders, Ea is the apparent activation energy, $R = 8.314\ \mathrm{J\cdot mol^{-1}\cdot K^{-1}}$ is the molar gas constant, T is the temperature variable in Kelvin, and β represents the heating rate settled experimentally.

3. Results and discussion

3.1. The MOF precursor and derived catalysts

As a precursor material for catalysts, the MOF needs to be analyzed first for its crystal structure and pyrolysis properties. Fig. 1(a) demonstrates the XRD pattern of the experimentally prepared Ce-UiO-66. Comparing the experimental and simulated results, the two patterns basically match, confirming that the prepared MOF precursor is as expected. The inset of Fig. 1(a) displays a schematic diagram of the Ce-UiO-66 topology, which has a cubic *Fd-3m* space group with fcc topology, consisting of $[Ce_6O_4(OH)_4]^{12+}$ bridged by 12 different BDC^{2-} to compose $[Ce_6O_4(OH)_4(BDC)_6]$ [28]. It was thermogravimetrically analyzed and the results are shown in Fig. 1(b). Organic frameworks have been completely removed from Ce-UiO-66 as the temperature increased to ~400 ℃, at which the mass loss was 63.3 %.

The four prepared catalysts were characterized by XRD to obtain crystal structure information and the results are shown in Fig. 1(c). The patterns of all types of catalysts were basically the same, with (111), (200), (220), (311), (222), (400), (331), and (420) crystal planes of the face-centered cubic CeO_2, as well as (111), (200), and (220) crystal planes of NiO, being observed [30]. According to the local magnified pattern in Fig. 1(d), diffraction peaks belonging to Co_3O_4 (311) were also found in Co-containing catalysts [31]. No additional diffraction peaks were found, implying that the prepared catalysts were free of impurities. In comparison of the NiO diffraction peaks of two monometallic catalysts, Ni/CeO_2-C and Ni/CeO_2-M, it was found that the peak intensity of MOF-derived catalyst was smaller than that of conventionally supported catalyst. Whereas the actual Ni loading was similar for both (see Table 1), which indicated that NiO particles were less crystallized and more dispersed in the MOF-derived catalyst system. The diffraction peaks of both NiO and Co_3O_4 in Co-containing catalysts also met the above features. The better spatial distribution of MNPs was achieved in the MOF-derived catalysts, which was attributed to the great dispersion of metal cations in the MOF precursor with high specific surface area.

The crystal size and lattice constant were calculated using Scherrer's equation and cubic lattice equation, respectively, and the results are shown in Table 1. For CeO_2 grain size, the MOF-derived catalysts were larger than the conventional catalysts, while the Ni-Co bimetallic systems were larger than the Ni monometallic ones. The grain size further affected the microscopic void structure, and the specific surface area was negatively correlated with the grain size. The textural information and

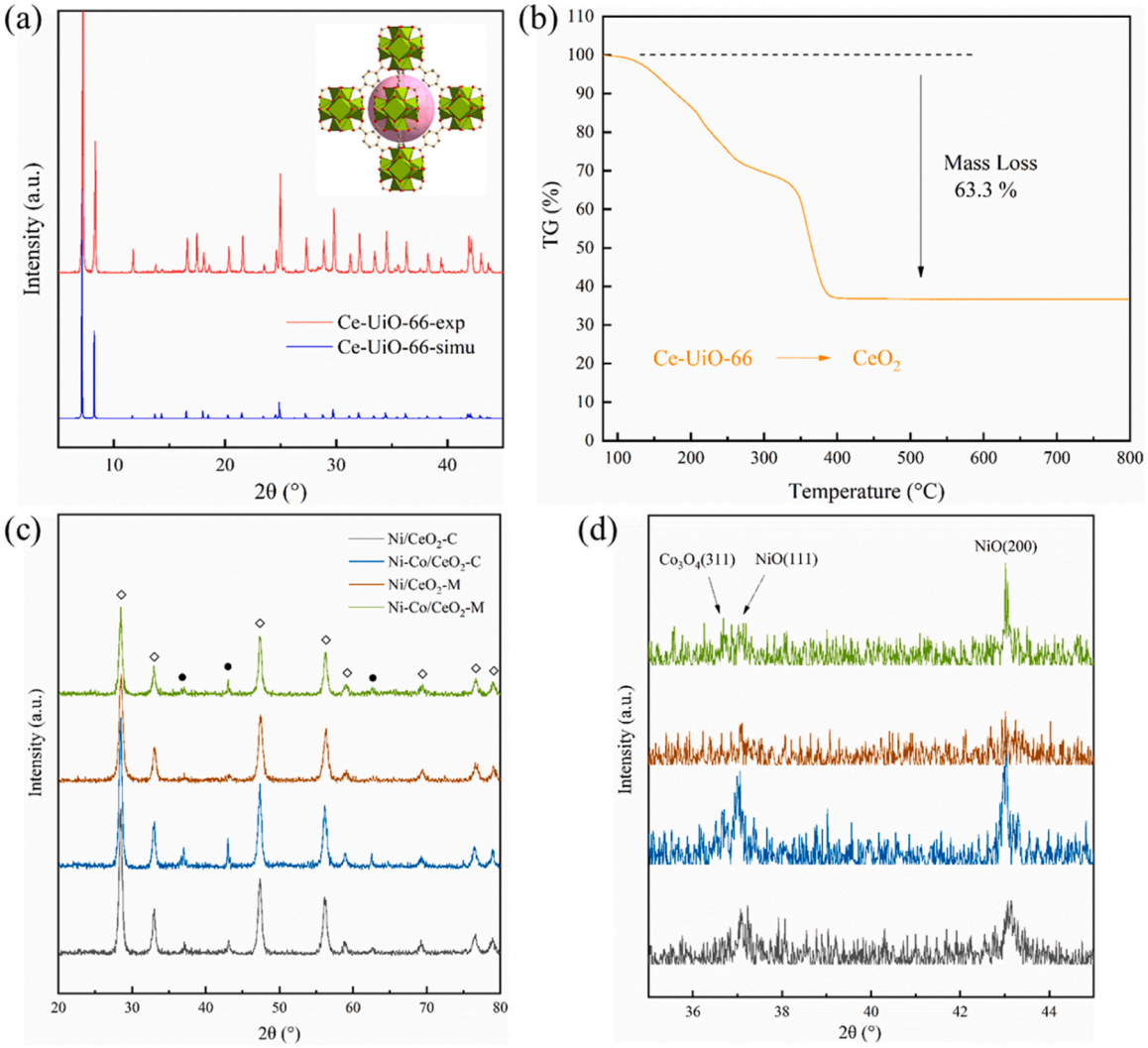

Fig. 1. MOF precursor analysis and XRD characterization of fresh catalysts: (a) experimental and simulated Ce-UiO-66 XRD patterns; (b) the TG curve of Ce-UiO-66 precursor calcined in air; (c) XRD patterns of fresh catalysts, and (d) their local enlargements.

Table 1
Metal loading and textural characterization of fresh catalysts.

Catalysts	Ni (wt%)[a]	Co (wt%)[a]	S_{BET} ($m^2 \bullet g^{-1}$)[b]	V_p ($cm^3 \bullet g^{-1}$)[c]	D_p (nm)[d]	a (Å)[e]	D_{CeO2} (nm)[f]	D_{NiO} (nm)[f]
Ni/CeO_2-C	9.51	-	30.65	0.12	11.74	5.4291	15.49	25.57
Ni-Co/CeO_2-C	9.84	4.76	24.93	0.10	12.14	5.4312	16.55	28.80
Ni/CeO_2-M	9.56	-	22.66	0.11	15.12	5.4179	16.94	17.23
Ni-Co/CeO_2-M	9.36	4.98	21.07	0.10	15.74	5.4221	17.29	23.73

[a] Measured by ICP-OES.
[b] Determined by BET method.
[c] Cumulative pore volume derived from the BJH desorption branch.
[d] Average pore diameter derived from the BJH desorption branch.
[e] Calculated from the cubic lattice formula based on XRD data.
[f] Calculated from the Scherrer's equation based on XRD data.

N_2 physisorption isotherm curves can be found in Table 1 and Supplementary Fig. S1. In addition, the lattice constants of MOF-derived catalysts were all found to be smaller than those of the corresponding conventionally supported catalysts, and the lattice constants of monometallic catalysts were smaller than those of the bimetallic ones. Lattice parameter shifts are evidence for solid solution formation [32,33]. For Ni-O-Ce solid solutions, the higher the Ni metal solubility, the smaller the CeO_2 lattice constant. This is due to the replacement of Ce ions (0.101 nm) by smaller radius Ni ions (0.072 nm) in the solid solution [34]. Changes in the XRD patterns from the MOF precursor to derived catalysts showed that the preparation process involved the removal of organic components and the reorganization of crystal cells. Metal ions highly dispersed on Ce-UiO-66 were dissolved in the newly formed CeO_2 lattice, resulting in a Ni-O-Ce solid solution structure. The difference in CeO_2 lattice constants between mono- and bimetallic catalysts was attributed to the generation of intermetallic interactions between Ni and

Co, which somewhat affected the dissolution of metal atoms in the CeO_2 lattice. In fact, the two elements Ni and Co, which are close in atomic mass and electronic structure, are prone to charge transfer and even form Ni-Co alloys [6,17,35].The difference in NiO grain size between mono- and bimetallic catalysts suggested that D_{NiO} was larger in Co-containing catalysts, giving evidence for cell-boundary distortion and microcrystalline growth. It was also observed that the NiO grain sizes of the MOF-derived catalysts were all smaller than those of the corresponding conventionally supported catalysts, which was still attributed to the spatial dispersion of MNPs.

3.2. Microstructure and XPS analysis of activated catalysts

HRTEM and HAADF-STEM were used to further observe the microstructure and elemental distribution of the pre-activated catalysts, as shown in Fig. 2. Lattice streaks of CeO_2 were clearly recognized in all catalysts. Since the Ni and Co lattice spacings are so close that it is not easy to identify them by lattice streaks, all metals identified were tentatively assigned to Ni. However, from the distribution of metal elements in the Co-containing catalysts (Fig. 2(b5) and (b6), Fig. 2(d5) and (d6)), the locations of Ni and Co were highly overlapping, which implies that the two existed in the catalyst system in a tightly contiguous form. Micro-scale spatial vicinity of Ni-Co provided the channel for intermetallic charge transfer and the basis for intermetallic interactions. The micrographs also showed that the metal nanoparticles of the conventional catalysts were relatively loose, and they did not constitute a strongly interconnected structure with the CeO_2 support. In contrast, in the MOF-derived catalysts, metal nanoparticles encapsulated by the thin layer of the support were observed (white dashed lines in Fig. 2(c2) and (d2)), which implies the formation of strong metal-support interactions.

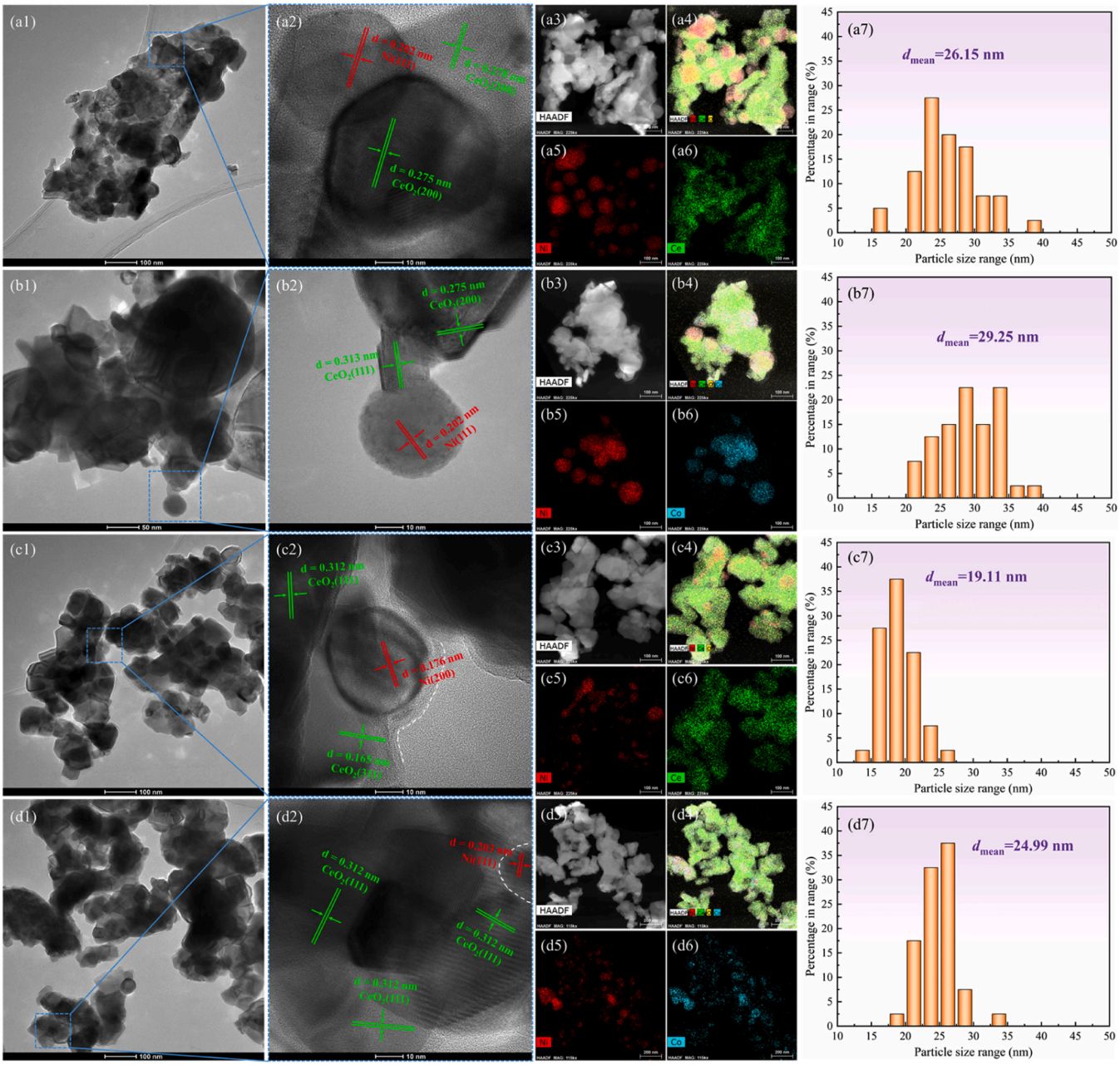

Fig. 2. HRTEM and HAADF-STEM were utilized to investigate the microstructure and elemental distribution of the different catalysts: (a) Ni/CeO_2-C, (b) Ni-Co/CeO_2-C, (c) Ni/CeO_2-M, and (d) Ni-Co/CeO_2-M; (x1–2) Electron microscope photographs, (x3–6) EDS elemental mapping images, (x7) statistical analysis of metal particle size distribution, x = a, b, c,d.

Moreover, the metal dispersion of the MOF-derived materials was much better compared to the conventional catalysts, as many agglomerated large particles were observed in the elemental mappings of the latter. In addition, the metal particle size distribution was statistically analyzed based on electron microscope pictures, as shown in Fig. 2(a7)-(d7). The metal particle sizes of the four catalysts followed Ni-Co/CeO_2-C > Ni/CeO_2-C > Ni-Co/CeO_2-M > Ni/CeO_2-M, which coincided with the results calculated by Scheller's equation. It was also found that the metal particle sizes of the MOF-derived catalysts were more uniform and exhibited narrow and tall features in the histograms, which further validated that the MOF-derived scheme helped to inhibit the growth and sintering of metal particles.

XPS characterization was performed to probe the surface chemical environment and elemental valence of pre-reduced catalysts, and the results are shown in Fig. 3. Many Ce^{3+}/Ce^{4+} pairs are present in the reduced CeO_2 support, so the Ce 3d energy spectrum in Fig. 3(a) can be decoupled into 10 split peaks. Among these, μ^0/ν^0 and μ'/ν' are attributed to Ce^{3+} species, while μ/ν, μ''/ν'', and μ'''/ν''' are associated with Ce^{4+} species. Fig. 3(b) shows the O 1 s spectrum including 3 distinct components. The O_L peak is attributed to lattice oxygen in metal oxides, the O_V peak is typically used to measure surface oxygen defects, and the O_C peak is assigned to surface-adsorbed oxygen species. In addition, the Ni $2p_{3/2}$ shown in Fig. 3(c) can also be split into 3 sub-peaks, which are Ni^0, Ni^{2+} and Ni satellite peaks. The relative content of Ce^{3+}, O_V, and Ni^0 were determined through the peak area method, which can be found in our previous study [27], and the results are displayed in Table 2.

Ce^{3+} contents were found to follow Ni-Co/CeO_2-M > Ni-Co/CeO_2-C > Ni/CeO_2-M > Ni/CeO_2-C. The surface oxygen vacancy concentration (O_V) exhibited a similar trend to the Ce^{3+} content, which coincides with the fact that the formation of oxygen defects in CeO_{2-x} is accompanied by a $Ce^{4+}\rightarrow Ce^{3+}$ valence transition. Compared to conventionally supported catalysts, MOF-derived catalysts have higher oxygen vacancy concentrations. This may be on the one hand related to the lattice defects resulting from the re-nucleation of metal clusters during the heat treatment of MOF materials. On the other hand, it was also attributed to the formation of Ni-O-Ce solid solution by Ni embedded in CeO_2, which increased the amount of reducible oxygen and oxygen vacancies [32,36]. The higher oxygen vacancy concentration of Ni-Co bimetallic catalysts compared to Ni monometallic catalysts was in agreement with the findings of previous reports [6]. Yadav et al. [37] revealed that Co-doped CeO_2 was helpful in decreasing the vacancy formation energy and could effectively improve the oxygen availability on the catalyst surface. Tang et al. [31] also confirmed the strong interaction between Co and CeO_2, and the Ce^{3+} and surface oxygen defects in Co-containing catalysts were significantly more than those in Ni monometallic catalysts. In addition, the contents of Ni^0 were in the order of Ni-Co/CeO_2-M > Ni/CeO_2-M > Ni-Co/CeO_2-C > Ni/CeO_2-C, implying that both MOF-derived synthesis and bimetallic system favored to increase the reducibility of metal particles. It was also noted that the introduction of Co resulted in a shift of the Ni^0 peak to the higher binding energy, which provided evidence for charge transfer and intermetallic interactions between Ni-Co [35,38]. Compared to the conventionally supported Ni-Co catalyst (0.14 eV), the intermetallic interactions were more intense in the MOF-derived one (0.19 eV). It was shown that the charge transfer between Ni and Co metals triggered the reassignment and non-uniform distribution of charge, which enhanced the charge transport efficiency from the catalyst surface to the adsorbed species [17]. This suggested that the MOF-derived bimetallic catalyst was more advantageous in modulating the intermetallic interaction and enhancing the site activity.

Table 2
The quantified elemental valence information extracted from the XPS analysis.

Catalysts	Ce^{3+} (%)	O_V (%)	Ni^0 (%)
Ni/CeO_2-C	21.49	22.54	19.68
Ni-Co/CeO_2-C	25.68	30.98	20.58
Ni/CeO_2-M	23.52	23.57	21.25
Ni-Co/CeO_2-M	27.82	33.68	23.09

3.3. Temperature programmed tests

To analyze the reducibility and CO_2 adsorption capacity, temperature programmed tests were carried out on the raw and reduced catalysts, respectively, as shown in Fig. 4. Fig. 4(a) shows the H_2-TPR results of the raw catalysts, where significant signals were observed in the ranges of 80–240, 240–400 and 650–800 °C. Depending on the genesis

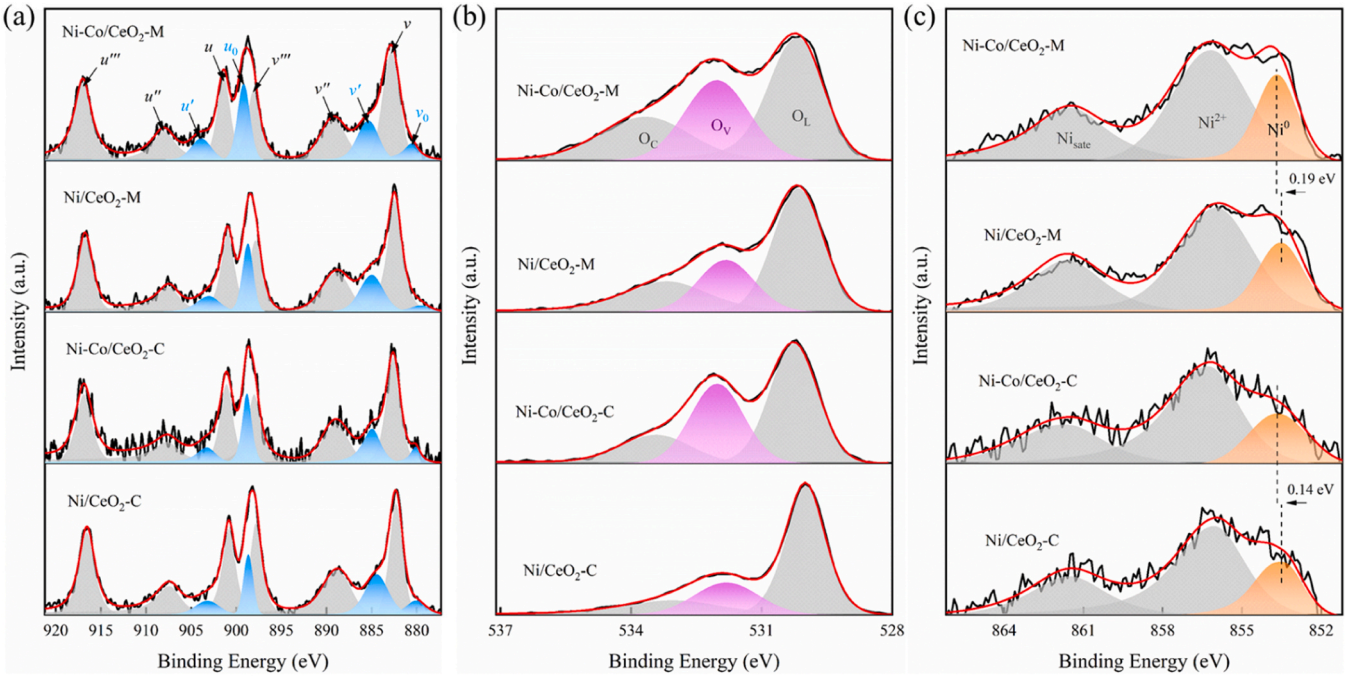

Fig. 3. XPS characterization of the catalysts in reducing state: (a) Ce 3d; (b) O 1 s; (c) Ni $2p_{3/2}$.

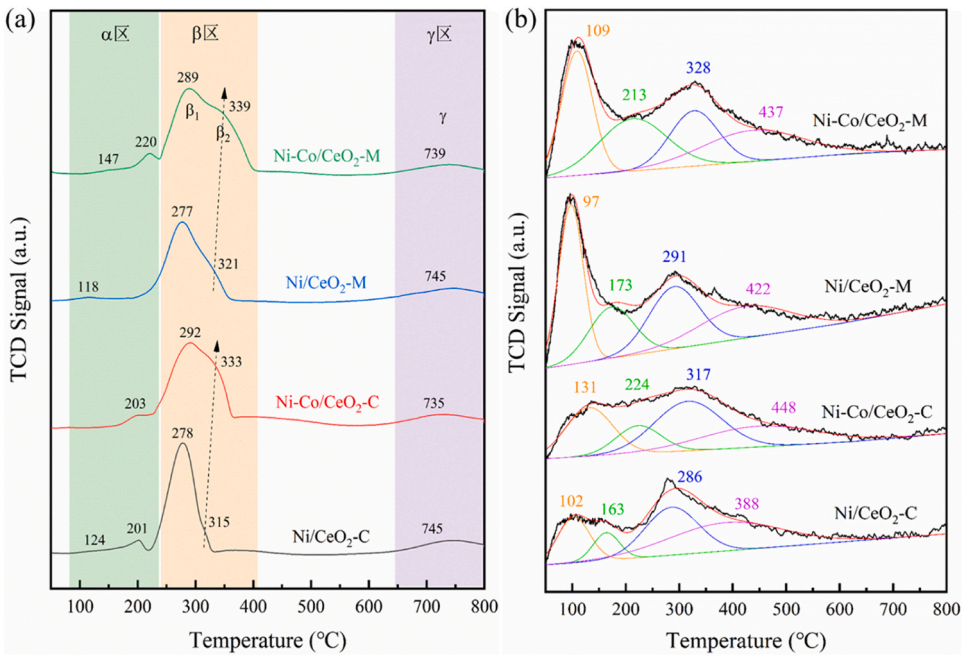

Fig. 4. Temperature programmed tests for different catalysts: (a) H_2-TPR for the raw catalyst; (b) CO_2-TPD for the reduced catalyst.

of the reduction peaks, the α, β and γ regions can be specifically defined [39,40]. Among them, peaks in the α-region are associated with the reduction of surface adsorbed oxygen species, such as surface -OH and O_2. Owing to the diversity of adsorbed species and adsorption strengths, multiple α peaks, corresponding to different reduction temperatures, are usually observed in this region [41]. The signal peaks in β-region are primarily ascribed to the reduction of metal oxides, with the reduction temperature being dependent on the intensity of MSI [41,42]. The reduction of metal cations, which interact weakly and strongly with the support, to metals in a lower valence state (e.g., $Ni^{2+} \rightarrow Ni^0$) can be classified as β_1 and β_2, respectively. Moreover, it has been verified that the co-reduction of surface CeO_2 took place within the β-peak region, in spite of the ambiguity of the curve, which was elusive to interpret [43]. The bulk reduction of CeO_2 is significantly more difficult than its surface reduction, hence the γ peaks ~740 °C are assigned to the reduction of bulk CeO_2 [40,41].

Although the H_2-TPR curves of the four catalysts shared a similar overall shape, there were differences in the details. Ni-Co/CeO_2-M showed higher α-peak intensities as well as reduction temperatures compared to the other catalysts, suggesting that this catalyst had more reactive oxygen species and greater adsorption strength. For the reduction peaks in the β-region, they were shifted towards higher reduction temperatures caused by both MOF-derived synthesis and Co doping. Comparing the β_1 peaks, the reduction temperatures of MOF-derived catalysts and conventional catalysts were not significantly different, while the peak intensities decreased; the reduction temperatures of the bimetallic catalysts appeared to be shifted to higher values in comparison with the monometallic catalysts, and the peak intensities also had a tendency to decrease. Comparing the β_2 peaks, both the MOF-derived synthesis and Co addition led to the increase in reduction temperature and enhancement of peak intensity. These provided sound evidence for enhanced metal-support as well as intermetallic interactions, consistent with XRD and XPS findings. The two interactions and their synergistic effects provided additional metal and metal-support interfacial sites for adsorption activation of reactant gases [6, 32].

Fig. 4(b) displays the CO_2-TPD curves of the catalysts after pre-activation, highlighting the basicity and CO_2 adsorption behavior on different catalyst surfaces. Four types of basic sites exist on the catalyst surface according to the division of basicity strength, i.e., weakly (50–150 °C), moderately (150–300 °C), strongly (300–500 °C) and extremely basic sites (>500 °C) [43]. Furthermore, depending on the surface adsorption category, peaks beneath ~420 °C are generally assigned to the desorption of CO_2 from bridged, monodentate, bidentate carbonates and carboxylates, while the more difficult desorption is thought to be related to multidentate carbonates [39,44].

The CO_2-TPD curves of the examined samples showed different features, and the MOF-derived synthesis had significant effects on the desorption peaks. The weakly basic range corresponded to the first desorption peak in Fig. 4(b). It can be seen that the peak intensities of MOF-derived catalysts were significantly increased compared to conventionally catalysts. This implies the presence of more weakly basic hydroxyl species on the catalyst surface, which are critical sites for providing surface oxygen circulation. The moderately basic range corresponded to the second and third peaks. The intensities of these two peaks showed that the MOF-derived catalysts were significantly larger than the conventional ones, indicating that the amount of CO_2 adsorbed on the surface of the former was much higher. This is attributed to the fact that the MOF-derived catalysts have a lot of metal-support interfaces facilitated by dispersed MNPs, as well as more surface oxygen defects, which provide key sites for CO_2 adsorption activation. In the strongly basic range, a fourth peak was observed, still exhibiting a greater peak intensity for MOF-derived catalysts. From the CO_2-TPD results, it was clear that the MOF-derived catalysts offered remarkable benefits in promoting CO_2 adsorption activation and reactive oxygen cycle. It was also noticed that, compared to the monometallic ones, the main feature of the bimetallic catalysts was the increase in desorption temperature, which was a manifestation of the enhanced surface basicity.

3.4. Catalytic performance assessment

DRM catalytic performance tests were performed on different catalysts to evaluate their respective capabilities. Fig. 5 shows the initial activity versus reaction temperature for different samples. The DRM activity of all catalysts increased with temperature, matching the inherent nature of an endothermic reaction. On the basis of the same preparation method, the activity of bimetallic catalyst was lower than

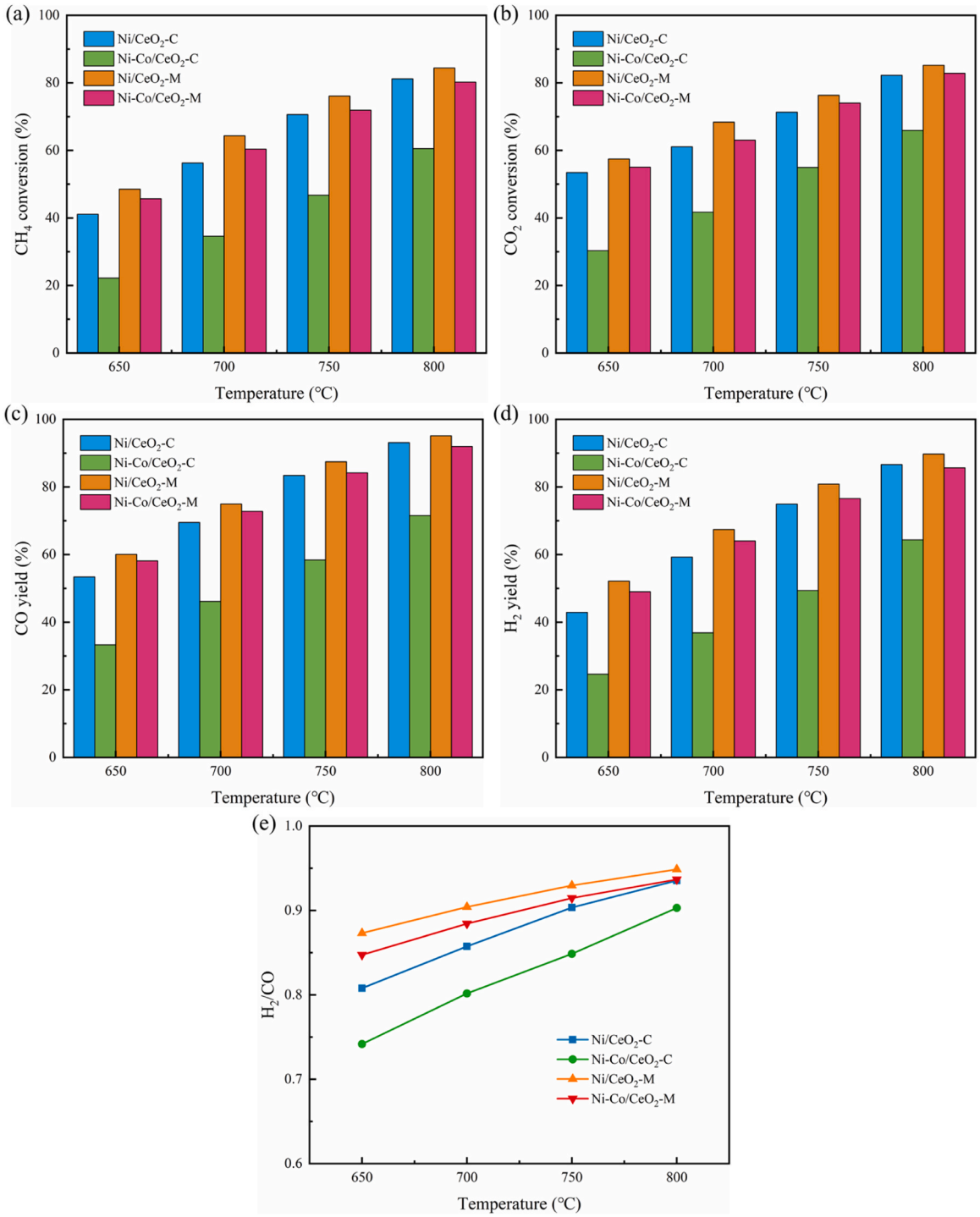

Fig. 5. Initial activity at varying reaction temperature: the conversion of (a) CH_4 and (b) CO_2, the yield of (c) CO and (d) H_2, (e) H_2/CO ratio. Experimental parameters: 100 mg catalyst, atmospheric pressure, CH_4:CO_2:N_2 = 1:1:3, GHSV = 36 L•h^{-1}•g^{-1}.

that of monometallic one, and it was considered that there were two main reasons for this. First, as shown by the textural information in Table 1, the addition of Co inevitably led to an increase in the particle size of active metal independent of the preparation method. Larger metal particle size implies deteriorated spatial dispersion, which reduces the exposure density of the active sites. Similar scenarios have been reported in previous studies [14,45,46]. Second, as an oxyphilic site, Co is beneficial to increase the oxygen concentration on catalyst surface, but it is also prone to irreversible oxidation of the active metal due to excessive adsorption of oxygen [6,15,47]. However, the metal particle size of the MOF-derived bimetallic catalyst Ni-Co/CeO_2-M (23.73 nm) was significantly smaller than that of the conventional bimetallic catalyst Ni-Co/CeO_2-C (28.80 nm), a feature that also applied to the Ni monometallic catalysts (17.23 nm vs. 25.57 nm). This suggests that the MOF-derived synthesis strategy contributed to the enhancement of MNPs dispersion, which could be attributed to the uniform diffusion of metal ions in the porous MOF precursor. Moreover, according to XPS Ni 2p analysis (Fig. 3(c)), the MOF-derived material promoted charge transfer between Ni-Co. It has been shown that this particular intermetallic interaction can effectively inhibit metal sintering and catalyst

re-oxidation [15,47,48]. So that, as visualized from the histograms (Fig. 5(a)-(d)), different from the conventional monometallic and bimetallic catalysts which had significant activity disparity, the activity gap between MOF-derived monometallic and bimetallic catalysts appeared to be small. It was also noticed that the activity of MOF-derived catalysts was higher than that of conventional catalysts, both for monometallic and bimetallic. In addition, H_2/CO ratios displayed in Fig. 5(e) also well matched the features mentioned above, i.e., the MOF-derived catalysts not only had higher ratios than the conventionally supported catalysts in both cases, but also showed smaller differences between the mono- and bimetallic catalysts. Actually, Co doping reduces the activation energy barrier of CO_2 by facilitating charge transfer from the catalytic surface to CO_2 [17]. However, this also enhances the reverse water gas shift (RWGS) side reaction, i.e., $CO_2 + H_2 \rightarrow CO + H_2O$, which is the main factor for the lower product ratio of Ni-Co/CeO_2-C. Comparison of H_2/CO ratios confirmed the potential of MOF-derived materials in inhibiting side reactions and improving product selectivity. In summary, it was considered that the proposed MOF derivatization approach not only improved the initial activity and product selectivity in DRM, but also effectively mitigated the side effects

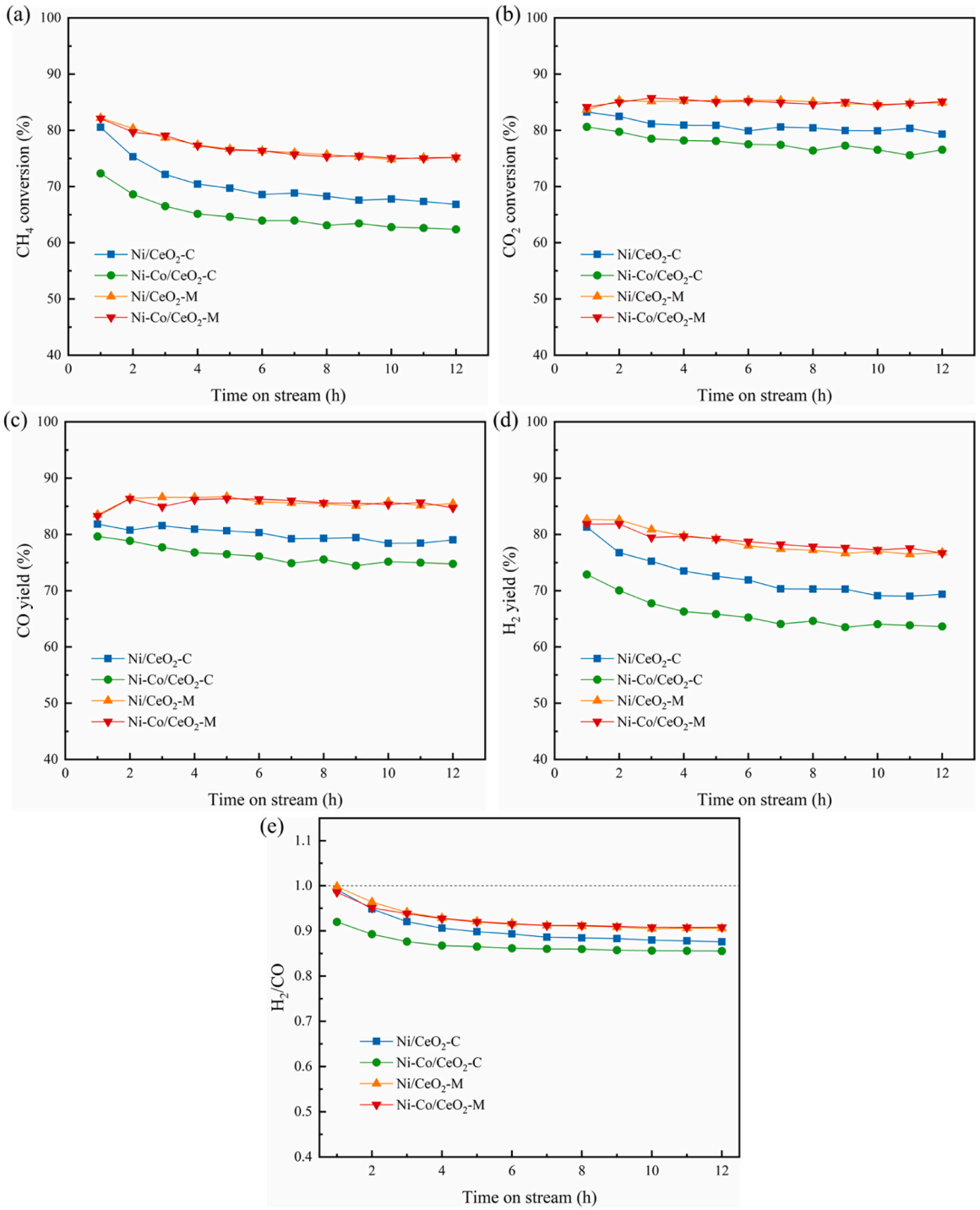

Fig. 6. Variation of reactivity with time on stream for different catalysts: the conversion of (a) CH_4 and (b) CO_2, the yield of (c) CO and (d) H_2, (e) H_2/CO ratio. Experimental parameters: 100 mg catalyst, atmospheric pressure, 700 ℃, CH_4:CO_2:N_2 = 1:1:3, GHSV = 36 L•h^{-1}•g^{-1}.

brought by the introduction of Co. Combined with the results of XRD, XPS and H_2-TPR, it should be attributed to the optimization of metal dispersion, intermetallic interactions and metal-support interface structure.

The variation of each indicator with reaction duration is shown in Fig. 6 to compare the DRM stability for different catalysts. The parallel experiments and error-bar analyses were performed in sampling manner (Fig. S2), thus validating the reliability and reproducibility of the catalytic performance data. Overall, the MOF-derived catalysts, i.e., Ni/CeO_2-M and Ni-Co/CeO_2-M were similar and the best in stability tests, Ni/CeO_2-C was the next, while Ni-Co/CeO_2-C was the worst. In particular, Fig. 6(a) illustrates the variation in CH_4 conversion, with Ni/CeO_2-C and Ni-Co/CeO_2-C showing a decrease of 13.7 % and 10.0 %, while Ni/CeO_2-M and Ni-Co/CeO_2-M decreased by 7.0 % and 6.9 %, respectively. As shown in Fig. 6(b), the changes in CO_2 conversion of Ni/CeO_2-C, Ni-Co/CeO_2-C, Ni-CeO_2-M, and Ni-Co/CeO_2-M were −3.9 %, −4.0 %, +1.2 %, and +1.0 %, in that order, after stability testing. For CO yield, as Fig. 6(c) shows, the variation of the four catalysts was −2.8 %, −4.9 %, +2.0 %, and +1.4 %, sequentially. It can be seen that the dissociative adsorption of CO_2 and the generation of CO product over the MOF-derived catalysts were enhanced rather than diminished after stability tests. Fig. 6(d) presents the variation of H_2 yield, which decreased by 11.9 %, 9.2 %, 5.9 %, and 5.2 % after the reaction of the four catalysts, respectively, also showing that the MOF-derived catalysts were more stable than the conventional ones. In addition, Fig. 6(e) illustrates the trend of H_2/CO molar ratio in products, which decreased by 0.12, 0.06, 0.09, and 0.08 for the four catalysts, and finally stabilized around 0.88, 0.86, 0.91, and 0.91, respectively.

Combining the changes in various indicators, the MOF-derived catalysts clearly had better DRM stability. Additionally, the catalytic stability test for Ni-Co/CeO_2-M was extended to 24 h, and still no significant deactivation was observed (Fig. S3). Notably, for CO_2 conversion and CO yield, no degradation in activity was observed during the long continuous reaction. According to Luisetto et al. [39], the DRM activity of CeO_2-based catalyst was closely related to MSI, surface oxygen defects, and basic sites favoring CO_2 adsorption. While Wang et al. [49] concluded that oxygen mobility was crucial in DRM process, and that active lattice oxygen migration involving oxygen vacancies facilitated the gasification of CHx species. Therefore, in conjunction with the previous analysis, the good catalytic stability of the prepared MOF-derived catalysts was likely attributed to the optimized metal-support interactions and surface defect sites, which enhanced the CO_2 activation and oxygen mobility. In addition, some catalysts similar to the system studied in this work were retrieved and the comparison results are shown in Table S1. It can be seen that the MOF-derived Ni-Co bimetallic catalyst presented in this study had a certain improvement in catalytic performance compared to similar materials. It was worth mentioning that the performance of Ni-Co/CeO_2-M even exceeded the results obtained by some materials at higher temperatures (750–800 °C).

3.5. FTIR and Raman characterization

To gain more insight into the intermediates and surface groups, the post-reaction catalysts were characterized by FTIR, which is shown in Fig. 7(a). Characteristic peaks were observed at 3432, 2370, 1635, 1390, 1059, 729, 638, 547, and 470 cm^{-1} in the FTIR spectra. Among them, the characteristic peaks at 3432, 1635 and 1390 cm^{-1} are ascribed to adsorbed H_2O molecules or surface -OH. The 2370 cm^{-1} peak is attributed to C-H stretching mode in hydrocarbons, and the peak located at 1059 cm^{-1} is assigned to the surface carbonate species. In addition, several peaks below 1000 cm^{-1} are relevant to the interatomic vibrations of metal oxides (e.g. CeO_2, NiO) [30,50,51]. By comparing the FTIR spectra, more surface adsorbed water molecules or hydroxyl groups were obviously present on the surface of the MOF-derived catalysts than those of the conventional ones, suggesting that a large amount of surface OH participated in reaction process as reactive oxygen species over the former. Zou et al. [15] confirmed that the OH active species on the Ni-Co bimetallic nanocatalyst reacted with CO_2 to form carbonate or bicarbonate species. While Omran et al. [52] revealed that OH* was the major oxidant of CH*, and its rate constant was second only to C* + O* in all carbon elimination reactions by using DFT method. Accordingly, the more OH species detected on the MOF-derived catalyst surface offered more active intermediates, thus contributing to CO_2 activation and carbon-containing species oxidation. In addition, stronger surface carbonate peaks at 1059 cm^{-1} were identified for the MOF-derived catalysts, which coincided with the results of CO_2-TPD.

Fig. 7(b) shows the Raman characterization results of post-reaction catalysts, focusing on the D and G bands involving surface carbon species. The peak around 1340 cm^{-1} is defined as the D-band, which is usually attributed to amorphous carbon or carbon atom lattice defects. While the peak around 1580 cm^{-1} is generated by the radial stretching vibration of sp^2 hybridized C-C bonds and belongs to the G-band [44,53]. The I_D/I_G value permits the measurement of the degree of surface carbon graphitization. It is accepted that a larger I_D/I_G value means more soft carbon that can be readily removed [43,54]. As illustrated in the inset of Fig. 7(b), the I_D/I_G ratios for the four catalysts, Ni/CeO_2-C, Ni-Co/CeO_2-C, Ni-CeO_2-M, and Ni-Co/CeO_2-M, were 0.234, 0.273, 0.256, and 0.302, respectively. Thus, MOF-derived Ni-Co bimetallic

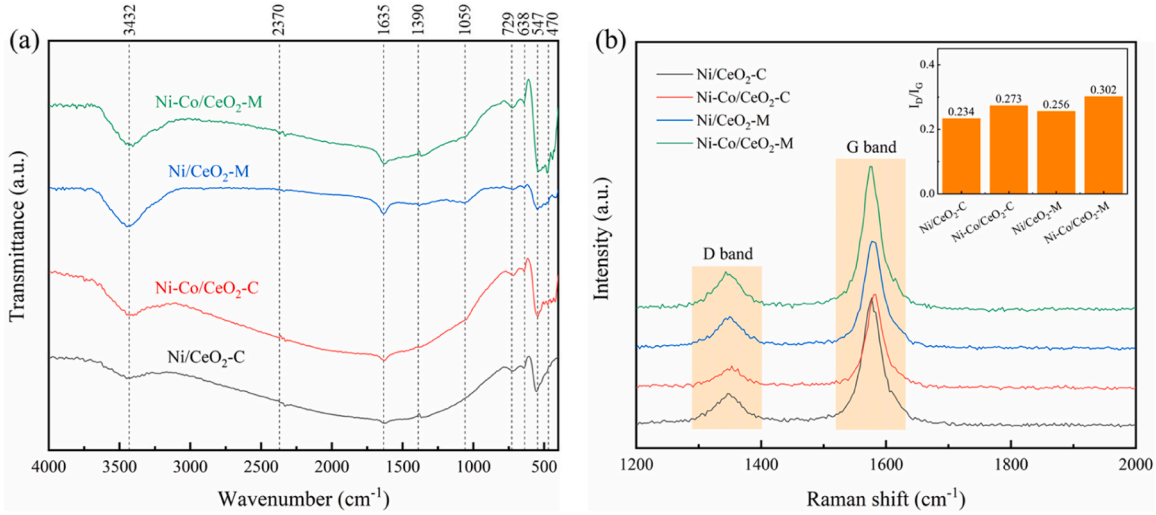

Fig. 7. FTIR and Raman characterizations of the post-reaction catalysts: (a) FTIR; (b) Raman.

catalysts were considered to have more active carbon species on the surface.

3.6. TG analysis and the kinetics of carbon gasification

The behavior of carbon formation and in-situ elimination directly affects the dynamic catalytic equilibrium, making it necessary to investigate the amount of carbon deposited and oxidation temperature. Carbon deposition on various catalysts was quantitatively assessed using TG analysis, with the results presented in Fig. 8(a). Ni-Co/CeO_2-C deposited the least amount of carbon among the four catalysts, which matched its inferior activity. The most carbon appeared on Ni/CeO_2-M, implying that the high DRM activity achieved by this catalyst was accompanied with carbon deposition. Whereas, Ni-Co/CeO_2-M was able to effectively inhibit coking while maintaining high catalytic activity. The structure of surface carbon species determines its oxidation temperature, which is lower for amorphous carbon compared to highly ordered graphitic carbon [39,43]. Thus, the differential curves were drawn beneath TG profiles to examine the variation in weight loss rate and carbon oxidation temperature of the post-reaction catalyst [39]. According to the dTG peaks, the maximum carbon oxidation rates of Ni/CeO_2-C, Ni-Co/CeO_2-C, Ni/CeO_2-M and Ni-Co/CeO_2-M appeared at 631 °C, 571 °C, 607 °C and 547 °C, respectively. The MOF-derived bimetallic catalyst not only exhibited the lowest carbon oxidation temperature, but also possessed a significantly higher carbon oxidation rate than the other three.

To further investigate the ability of different catalysts in eliminating surface carbon species, the carbon gasification behavior and kinetic characteristics in the DRM-like condition were explored using a modified Wigner-Polanyi method [3]. The post-reaction catalyst was oxidized in a pure CO_2 stream at different ramping rates, and the kinetic fitting was performed by the temperature T_M corresponding to the maximum carbon gasification rate, and the results are presented in Fig. 8(b). The apparent activation energies of carbon gasification were obtained as 128.2, 94.4, 111.5 and 89.2 kJ/mol for Ni/CeO_2-C, Ni-Co/CeO_2-C, Ni/CeO_2-M and Ni-Co/CeO_2-M, in that order. It was noted that the Ea of the MOF-derived catalyst was below that of the corresponding conventionally supported catalyst, and the Ni-Co bimetallic catalysts also showed lower activation energies compared to the Ni monometallic ones. Among all catalysts, Ni-Co/CeO_2-AM possessed the best carbon gasification kinetics, which provided the explanation for its good catalytic activity and stability.

The exact mechanism for the elimination of carbon species from the catalyst surface during the DRM process has received much attention. It was shown that two pathways, activated lattice oxygen in ceria support and surface adsorbed oxygen, jointly contributed to the conversion of surface carbon [55]. Zhang et al. [56] suggested that CO generation over CeO_2-supported catalysts mainly followed the MvK and L-H mechanisms, with the additional possibility of an E-R route. In this study, according to the H_2-TPR tests and XPS results, the MOF-derived bimetallic catalyst exhibited better reducibility and also formed more surface oxygen defects after pre-activation, which provided conditions for CO_2 dissociative adsorption as well as active lattice oxygen migration. The CO_2-TPD and FTIR results confirmed the presence of more surface carbonate and OH species on Ni-Co/CeO_2-M, the latter has been proven to be the important reactive oxygen species and intermediates during DRM reaction [15,52]. Therefore, one can infer that the MOF-derived Ni-Co bimetallic catalyst effectively facilitated two potential pathways for the removal of surface carbon species after the CO_2 adsorption activation step. As shown by the yellow dashed arrows in Scheme 1: (i) free reactive oxygen species, such as O* and OH*, underwent surface adsorption interspecies reaction via the L-H mechanism (C* + O* → CO* or C* + OH* → CHO*); (ii) the reactive lattice oxygen migration route engaged by oxygen vacancies promoted the surface carbon oxidation through the Mvk mechanism (C* + O_L → CO*), which was coincidental with the mechanism of oxygen vacancy-reactive lattice oxygen cycle proposed in our previous study [57].

4. Conclusions

In this work, the MOF material was shown to be available for active site modulation and interfacial structure optimization of bimetallic-supported catalysts. Ni-Co/CeO_2-M was synthesized by in situ impregnation using Ce-UiO-66 as a precursor. The abundant ordered pores and large specific surface area of the MOF substrate enabled great dispersion of metal ions, and the Ni-O-Ce solid solution structure and charge transfer between Ni-Co were induced in the subsequent controlled pyrolysis. Enhanced metal-support interactions and intermetallic interactions provided the catalyst interfacial modification, and the characterization of surface physicochemical properties confirmed the advantages of the MOF-derived Ni-Co bimetallic catalyst in terms of oxygen vacancy concentration, reducibility, and CO_2 activation capacity. Compared with conventional catalysts, the MOF-derived materials exhibited better DRM reactivity with no degradation of CO_2 conversion and CO yield observed during catalytic stability tests. More surface OH and carbonate species were found on Ni-Co/CeO_2-M, whose surface carbon featured a lower oxidation temperature and favorable gasification kinetics. Therefore, it was concluded that the proposed MOF-derived synthesis strategy not only contributed to the improvement of Ni-Co bimetallic synergism, but also promoted the availability and mobility of reactive oxygen species, thus effectively accelerating the conversion of carbon-containing intermediates. The significance of this

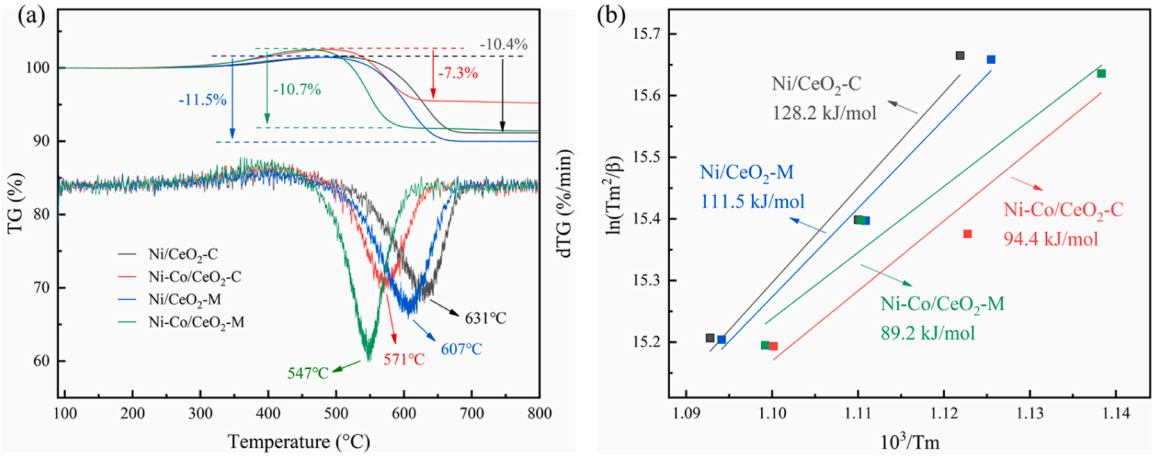

Fig. 8. The analysis of carbon deposits on the spent catalyst: (a) TG and dTG curves; (b) kinetic analysis of carbon gasification.

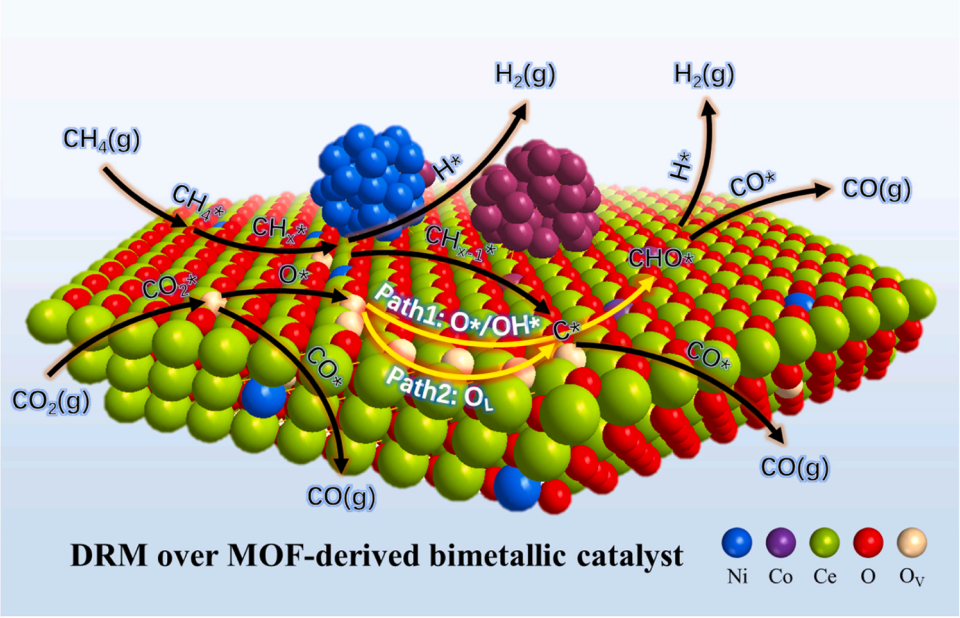

Scheme 1. A schematic representation of the DRM process catalyzed by the MOF-derived Ni-Co bimetallic catalyst.

work is to offer insights into the interfacial structure modification and anti-coking design of DRM catalysts.

Given the topological programmability and customizable coordination environments of MOFs, further developments in atomic-level fine-tuning of bimetallic sites and nanopore confinement effects are expected. The pretreatment process of MOF-derived materials is also worth exploring, including high-temperature calcination, chemical treatment, and atmosphere induction, which can directly affect the metal synergism and interfacial stability. Moreover, as common improvements, more rational metal formulations (e.g., metal type and content) deserve further investigation. The above prospects can be extended to different bi-/multimetallic catalyst systems, and it is believed that MOFs-derived materials have promising applications in the future.

CRediT authorship contribution statement

Xiong Junchang: Visualization, Investigation, Data curation. **Huang Zehua:** Methodology, Investigation. **Liu Hongchuan:** Writing – original draft, Visualization, Methodology, Investigation, Formal analysis, Conceptualization. **Dong Meirong:** Writing – review & editing, Validation, Project administration, Funding acquisition. **Liang Youcai:** Writing – review & editing, Funding acquisition. **Lu Jidong:** Writing – review & editing, Funding acquisition.

Declaration of Competing Interest

The authors declare that they have no known competing financial interests or personal relationships that could have appeared to influence the work reported in this paper.

Acknowledgments

This work was supported by National Natural Science Foundation of China (No. 52376107), Foundation of Science and Technology Projects in Guangzhou (2025A04J7048) and the Fundamental Research Funds for the Central Universities (2022ZFJH04). We also acknowledge the supports from Guangdong Province Key Laboratory of Efficient and Clean Energy Utilization (2013A061401005).

Appendix A. Supporting information

Supplementary data associated with this article can be found in the online version at doi:10.1016/j.jece.2025.116948.

Data Availability

Data will be made available on request.

References

[1] M.D. Garba, M. Usman, S. Khan, F. Shehzad, A. Galadima, M.F. Ehsan, A. S. Ghanem, M. Humayun, CO_2 towards fuels: a review of catalytic conversion of carbon dioxide to hydrocarbons, J. Environ. Chem. Eng. 9 (2021) 104756, https://doi.org/10.1016/j.jece.2020.104756.

[2] Z. Alipour, V.B. Borugadda, H. Wang, A.K. Dalai, Syngas production through dry reforming: a review on catalysts and their materials, preparation methods and reactor type, Chem. Eng. J. 452 (2023) 139416, https://doi.org/10.1016/j.cej.2022.139416.

[3] D. Guo, M.S. Li, Y. Lu, Y.F. Zhao, M.J. Li, Y.J. Zhao, S.P. Wang, X.B. Ma, Enhanced thermocatalytic stability by coupling nickel step sites with nitrogen heteroatoms for dry reforming of methane, ACS Catal. 12 (2022) 316–330, https://doi.org/10.1021/acscatal.1c04004.

[4] J.J. Torrez-Herrera, S.A. Korili, A. Gil, Recent progress in the application of Ni-based catalysts for the dry reforming of methane, Catal. Rev. Sci. Eng. 65 (2021) 1300–1357, https://doi.org/10.1080/01614940.2021.2006891.

[5] J.C. Seo, E. Cho, J. Kim, S.B. Kim, J.R. Youn, D.H. Kim, P.K. Ramasamy, K. Lee, C. H. Ko, Bifunctional metal doping engineering of Ni-supported alumina catalyst for dry methane reforming, J. Environ. Chem. Eng. 10 (2022) 108058, https://doi.org/10.1016/j.jece.2022.108058.

[6] E.S. Yang, E. Nam, Y. Jo, K.J. An, Coke resistant NiCo/CeO_2 catalysts for dry reforming of methane derived from core@shell Ni@Co nanoparticles, Appl. Catal. B-Environ. 339 (2023) 123152, https://doi.org/10.1016/j.apcatb.2023.123152.

[7] X.Z. Fang, L. Mao, L.J. Xu, J.T. Shen, J.W. Xu, X.L. Xu, X. Wang, Ni-Fe/La_2O_3 bimetallic catalysts for methane dry reforming: elucidating the role of Fe for improving coke resistance, Fuel 357 (2024) 129950, https://doi.org/10.1016/j.fuel.2023.129950.

[8] J.Y. Wang, Y. Fu, W.B. Kong, S.Q. Li, C.K. Yuan, J.R. Bai, X. Chen, J. Zhang, Y. H. Sun, Investigation of atom-level reaction kinetics of carbon-resistant bimetallic NiCo-reforming catalysts: combining microkinetic modeling and density functional theory, ACS Catal. 12 (2022) 4382–4393, https://doi.org/10.1021/acscatal.2c00027.

[9] D.S. Cao, C. Luo, Z.Q. Tan, T. Luo, Z.W. Shi, F. Wu, X.S. Li, Y. Zheng, L.Q. Zhang, Carbon deposition properties and regeneration performance of La_2NiO_4 perovskite oxide for dry reforming of methane, J. Environ. Chem. Eng. 11 (2023) 111022, https://doi.org/10.1016/j.jece.2023.111022.

[10] M.J. Yu, Y.A. Zhu, Y. Lu, G.S. Tong, K.K. Zhu, X.G. Zhou, The promoting role of Ag in Ni-CeO_2 catalyzed CH_4-CO_2 dry reforming reaction, Appl. Catal. B-Environ. 165 (2015) 43–56, https://doi.org/10.1016/j.apcatb.2014.09.066.

[11] D.G. Araiza, D.G. Arcos, A. Gomez-Cortes, G. Diaz, Dry reforming of methane over Pt-Ni/CeO_2 catalysts: effect of the metal composition on the stability, Catal. Today 360 (2021) 46–54, https://doi.org/10.1016/j.cattod.2019.06.018.
[12] T. Odedairo, J. Ma, J.L. Chen, S.B. Wang, Z.H. Zhu, Influences of doping Cr/Fe/Ta on the performance of Ni/CeO_2 catalyst under microwave irradiation in dry reforming of CH_4, J. Solid State Chem. 233 (2016) 166–177, https://doi.org/10.1016/j.jssc.2015.10.025.
[13] P.K. Yadav, P. Verma, S. Sharma, Bimetal (CuNi and CuCo) substituted CeO_2: an approach for low temperature dry reforming of methane, Mol. Catal. 565 (2024) 114398, https://doi.org/10.1016/j.mcat.2024.114398.
[14] I. Luisetto, S. Tuti, E. Di Bartolomeo, Co and Ni supported on CeO_2 as selective bimetallic catalyst for dry reforming of methane, Int. J. Hydrog. Energy 37 (2012) 15992–15999, https://doi.org/10.1016/j.ijhydene.2012.08.006.
[15] Z.P. Zou, T. Zhang, L. Lv, W.X. Tang, G.Q. Zhang, R.K. Gupta, Y. Wang, S.W. Tang, Preparation adjacent Ni-Co bimetallic nano catalyst for dry reforming of methane, Fuel 343 (2023) 128013, https://doi.org/10.1016/j.fuel.2023.128013.
[16] H. Ay, D. Uner, Dry reforming of methane over CeO_2 supported Ni, Co and Ni-Co catalysts, Appl. Catal. B-Environ. 179 (2015) 128–138, https://doi.org/10.1016/j.apcatb.2015.05.013.
[17] Z.L. Ou, J.Y. Ran, H.Y. Qiu, X. Huang, C.L. Qin, Understanding the role of Co segregation on the carbon deposition over Ni-Co bimetal catalyst in dry reforming of methane, Sep. Purif. Technol. 333 (2024) 125868, https://doi.org/10.1016/j.seppur.2023.125868.
[18] A.F. Sahayaraj, H.J. Prabu, J. Maniraj, M. Kannan, M. Bharathi, P. Diwahar, J. Salamon, Metal-organic frameworks (MOFs): the next generation of materials for catalysis, gas storage, and separation, J. Inorg. Organomet. Polym. Mater. 33 (2023) 1757–1781, https://doi.org/10.1007/s10904-023-02657-1.
[19] T. De Villenoisy, X.R. Zheng, V.N. Wong, S.S. Mofarah, H. Arandiyan, Y. Yamauchi, P. Koshy, C.C. Sorrell, Principles of design and synthesis of metal derivatives from MOFs, Adv. Mater. 35 (2023) 2210166, https://doi.org/10.1002/adma.202210166.
[20] Y.P. Xue, G.C. Zhao, R.Y. Yang, F. Chu, J. Chen, L. Wang, X.B. Huang, 2D metal-organic framework-based materials for electrocatalytic, photocatalytic and thermocatalytic applications, Nanoscale 13 (2021) 3911–3936, https://doi.org/10.1039/d0nr09064f.
[21] S. Sanati, R. Abazari, J. Albero, A. Morsali, H. García, Z.B. Liang, R.Q. Zou, Metal-organic framework derived bimetallic materials for electrochemical energy storage, Angew. Chem. -Int. Ed. 60 (2021) 11048–11067, https://doi.org/10.1002/anie.202010093.
[22] R.M. Rego, M.D. Kurkuri, M. Kigga, A comprehensive review on water remediation using UiO-66 MOFs and their derivatives, Chemosphere 302 (2022) 134845, https://doi.org/10.1016/j.chemosphere.2022.134845.
[23] E.P. Komarala, A.A. Dabbawala, M. Harfouche, M.A. Vasiliades, N. Charisiou, D. H. Anjum, S. Mao, M. Rueping, M.A. Baker, M.A. Goula, A.M. Efstathiou, K. Polychronopoulou, Tune and turn the pyrolysis of metal organic frameworks towards stable supported nickel catalysts for the dry reforming of methane, Appl. Surf. Sci. 666 (2024) 160388, https://doi.org/10.1016/j.apsusc.2024.160388.
[24] J.Y. Tu, C.H. Shen, D.H. Tsai, C.W. Kung, Carbonized nickel-incorporated metal-organic frameworks for methane reforming: Post-synthetic modification vs impregnation, ACS Appl. Nano Mater. 6 (2023) 10269–10279, https://doi.org/10.1021/acsanm.3c01173.
[25] R.D. Alli, R.F. Zhou, M. Mohamedali, N. Mahinpey, Effect of thermal treatment conditions on the stability of MOF-derived Ni/CeO_2 catalyst for dry reforming of methane, Chem. Eng. J. 466 (2023) 143242, https://doi.org/10.1016/j.cej.2023.143242.
[26] R.D. Alli, N. Mahinpey, Influence of organic ligand and nickel loading on the performance of MOF-derived catalysts for dry reforming of methane, Fuel 361 (2024) 130756, https://doi.org/10.1016/j.fuel.2023.130756.
[27] H.C. Liu, M.R. Dong, J.C. Xiong, Z.H. Huang, H.M. Hou, Y.C. Liang, J.D. Lu, Study on Ce-MOF-derived oxides as morphology-tunable catalyst supports for dry reforming of methane, Appl. Surf. Sci. 679 (2025) 161167, https://doi.org/10.1016/j.apsusc.2024.161167.
[28] M. Lammert, M.T. Wharmby, S. Smolders, B. Bueken, A. Lieb, K.A. Lomachenko, D. De Vos, N. Stock, Cerium-based metal organic frameworks with UiO-66 architecture: synthesis, properties and redox catalytic activity, Chem. Commun. 51 (2015) 12578–12581, https://doi.org/10.1039/c5cc02606g.
[29] T. Osaki, T. Mori, Kinetics of the reverse-Boudouard reaction over supported nickel catalysts, React. Kinet. Catal. Lett. 89 (2006) 333–339, https://doi.org/10.1007/s11144-006-0145-9.
[30] X.L. Yan, T. Hu, P. Liu, S. Li, B.R. Zhao, Q. Zhang, W.Y. Jiao, S. Chen, P.F. Wang, J. J. Lu, L.M. Fan, X.N. Deng, Y.X. Pan, Highly efficient and stable Ni/CeO_2-SiO_2 catalyst for dry reforming of methane: effect of interfacial structure of Ni/CeO_2 on SiO_2, Appl. Catal. B-Environ. 246 (2019) 221–231, https://doi.org/10.1016/j.apcatb.2019.01.070.
[31] Z.C. Tang, H.T. Cao, Y.H. Tao, H.J. Heeres, P.P. Pescarmona, Transfer hydrogenation from glycerol over a Ni-Co/CeO_2 catalyst: a highly efficient and sustainable route to produce lactic acid, Appl. Catal. B-Environ. 263 (2020) 118273, https://doi.org/10.1016/j.apcatb.2019.118273.
[32] R. Khatun, N. Siddiqui, R.S. Pal, S. Bhandari, T.S. Khan, S. Singh, M.K. Poddar, C. Samanta, R. Bal, Low temperature reforming of methane with CO_2 over Pt/CeO_2, Ni/CeO_2 and Pt-Ni/CeO_2 catalysts prepared by a solution-combustion method, Catal. Sci. Technol. 13 (2023) 6431–6445, https://doi.org/10.1039/d3cy00600j.
[33] A. Singhania, S.M. Gupta, Nickel nanocatalyst ex-solution from ceria-nickel oxide solid solution for low temperature CO oxidation, J. Nanosci. Nanotechnol. 18 (2018) 4614–4620, https://doi.org/10.1166/jnn.2018.15342.
[34] S. Xu, X.B. Yan, X.L. Wang, Catalytic performances of NiO-CeO_2 for the reforming of methane with CO_2 and O_2, Fuel 85 (2006) 2243–2247, https://doi.org/10.1016/j.fuel.2006.03.022.
[35] J.Q. Zhang, K. Xie, Y.C. Jiang, M. Li, X.J. Tan, Y. Yang, X.L. Zhao, L. Wang, Y. F. Wang, X.Y. Wang, Y.Z. Zhu, H.J. Chen, M.B. Wu, H.Q. Sun, S.B. Wang, Photoinducing different mechanisms on a Co-Ni bimetallic alloy in catalytic dry reforming of methane, ACS Catal. 13 (2023) 10855–10865, https://doi.org/10.1021/acscatal.3c02525.
[36] P.K. Yadav, S. Sharma, Ni, Co & Cu substituted CeO_2: a catalyst that improves H_2/CO ratio in the dry reforming of methane, Fuel 358 (2024) 130163, https://doi.org/10.1016/j.fuel.2023.130163.
[37] P.K. Yadav, K. Patrikar, A. Mondal, S. Sharma, Ni/Co in and on CeO_2: a comparative study on the dry reforming reaction, Sustain. Energ. Fuels 7 (2023) 3853–3870, https://doi.org/10.1039/d3se00649b.
[38] Z.L. Li, J.J. Chen, Y. Xie, J.J. Wen, H.L. Weng, M.X. Wang, J.Y. Zhang, J.Y. Cao, G. C. Tian, Q.L. Zhang, P. Ning, Zonal activation of molecular carbon dioxide and hydrogen over dual sites Ni-Co-MgO catalyst for CO_2 methanation: synergistic catalysis of Ni and Co species, J. Energy Chem. 91 (2024) 213–225, https://doi.org/10.1016/j.jechem.2023.12.027.
[39] I. Luisetto, S. Tuti, C. Romano, M. Boaro, E. Di Bartolomeo, J.K. Kesavan, S.M. S. Kumar, K. Selvakumar, Dry reforming of methane over Ni supported on doped CeO_2: new insight on the role of dopants for CO_2 activation, J. CO2 Util. 30 (2019) 63–78, https://doi.org/10.1016/j.jcou.2019.01.006.
[40] R. Tang, N. Ullah, Y.J. Hui, X. Li, Z.H. Li, Enhanced CO_2 methanation activity over Ni/CeO_2 catalyst by one-pot method, Mol. Catal. 508 (2021) 111602, https://doi.org/10.1016/j.mcat.2021.111602.
[41] S.M. Lee, Y.H. Lee, D.H. Moon, J.Y. Ahn, D.D. Nguyen, S.W. Chang, S.S. Kim, Reaction mechanism and catalytic impact of Ni/CeO_{2-x} catalyst for low-temperature CO_2 methanation, Ind. Eng. Chem. Res. 58 (2019) 8656–8662, https://doi.org/10.1021/acs.iecr.9b00983.
[42] M.S. Li, H. Amari, A.C. van Veen, Metal-oxide interaction enhanced CO_2 activation in methanation over ceria supported nickel nanocrystallites, Appl. Catal. B-Environ. 239 (2018) 27–35, https://doi.org/10.1016/j.apcatb.2018.07.074.
[43] Z.Z. Qin, L.Y. Chen, J. Chen, T.M. Su, H.B. Ji, Ni/CeO_2 prepared by improved polyol method for DRM with highly dispersed Ni, Greenh. Gases 11 (2021) 1245–1264, https://doi.org/10.1002/ghg.2129.
[44] F.G. Wang, K.H. Han, W.S. Yu, L. Zhao, Y. Wang, X.J. Wang, H. Yu, W.D. Shi, Low temperature CO_2 reforming with methane reaction over CeO_2-modified Ni@SiO_2 catalysts, ACS Appl. Mater. Interfaces 12 (2020) 35022–35034, https://doi.org/10.1021/acsami.0c09371.
[45] L.H. Lyu, M. Shengene, Q.X. Ma, J. Sun, X.H. Gao, H. Fan, J.L. Zhang, T.S. Zhao, Synergy of macro-meso bimodal pore and Ni-Co alloy for enhanced stability in dry reforming of methane, Fuel 310 (2022) 122375, https://doi.org/10.1016/j.fuel.2021.122375.
[46] B. Li, X.Q. Yuan, L.Y. Li, X.J. Wang, B.T. Li, Stabilizing Ni-Co alloy on bimodal mesoporous alumina to enhance carbon resistance for dry reforming of methane, Ind. Eng. Chem. Res. 60 (2021) 16874–16886, https://doi.org/10.1021/acs.iecr.1c02164.
[47] W. Tang, J.P. Cao, C.C. Chen, W. Jiang, C.X. Chen, Z.M. He, K.R. Luan, X.Y. Zhao, Lignite-char-supported highly dispersed ultrasmall Ni-Co alloy for stably dry reforming of methane at low temperature, Chem. Eng. Sci. 281 (2023) 119165, https://doi.org/10.1016/j.ces.2023.119165.
[48] B. Erdogan, H. Arbag, N. Yasyerli, SBA-15 supported mesoporous Ni and Co catalysts with high coke resistance for dry reforming of methane, Int. J. Hydrog. Energy 43 (2018) 1396–1405, https://doi.org/10.1016/j.ijhydene.2017.11.127.
[49] N. Wang, W.Z. Qian, W. Chu, F. Wei, Crystal-plane effect of nanoscale CeO_2 on the catalytic performance of Ni/CeO_2 catalysts for methane dry reforming, Catal. Sci. Technol. 6 (2016) 3594–3605, https://doi.org/10.1039/c5cy01790d.
[50] S. Aghamohammadi, M. Haghighi, M. Maleki, N. Rahemi, Sequential impregnation vs. sol-gel synthesized Ni/Al_2O_3-CeO_2 nanocatalyst for dry reforming of methane: effect of synthesis method and support promotion, Mol. Catal. 431 (2017) 39–48, https://doi.org/10.1016/j.mcat.2017.01.012.
[51] N. Rahemi, M. Haghighi, A.A. Babaluo, M.F. Jafari, P. Estifaee, CO_2 reforming of CH_4 over CeO_2-doped Ni/Al_2O_3 nanocatalyst treated by non-thermal plasma, J. Nanosci. Nanotechnol. 13 (2013) 4896–4908, https://doi.org/10.1166/jnn.2013.7585.
[52] A. Omran, S.H. Yoon, M. Khan, M. Ghouri, A. Chatla, N. Elbashir, Mechanistic insights for dry reforming of methane on Cu/Ni bimetallic catalysts: DFT-assisted microkinetic analysis for coke resistance, Catalysts 10 (2020) 1043, https://doi.org/10.3390/catal10091043.
[53] A.L.A. Marinho, R.C. Rabelo-Neto, F. Epron, N. Bion, F.S. Toniolo, F.B. Noronha, Embedded Ni nanoparticles in $CeZrO_2$ as stable catalyst for dry reforming of methane, Appl. Catal. B-Environ. 268 (2020) 118387, https://doi.org/10.1016/j.apcatb.2019.118387.
[54] F.Z. Mohammad, I. Ahmad, J.J. Siddiqui, K.M. Ali, M. Mudsar, H. Arshad, Light weight RGO/Fe_3O_4 nanocomposite for efficient electromagnetic absorption coating in X-band, J. Mater. Sci. Mater. Electron 29 (2018) 19775–19782, https://doi.org/10.1007/s10854-018-0103-0.
[55] C.M. Damaskinos, J. Zavasnik, P. Djinovic, A.M. Efstathiou, Dry reforming of methane over Ni/$Ce_{0.8}Ti_{0.2}O_{2-delta}$: the effect of Ni particle size on the carbon

pathways studied by transient and isotopic techniques, Appl. Catal. B-Environ. 296 (2021) 120321, https://doi.org/10.1016/j.apcatb.2021.120321.

[56] Z.Y. Zhang, T. Xie, In situ DRIFTs-based comprehensive reaction mechanism of photo-thermal synergetic catalysis for dry reforming of methane over Ru-CeO_2 catalyst, J. Colloid Interface Sci. 677 (2025) 863–872, https://doi.org/10.1016/j.jcis.2024.08.019.

[57] H.C. Liu, M.R. Dong, J.C. Xiong, J.S. Yang, J.Y. Ning, Y.C. Liang, J.D. Lu, CO_2 laser promoted oxygen vacancy-active oxygen cycle in DRM on Ni/CeO_2, Energy Conv. Manag. 286 (2023) 117081, https://doi.org/10.1016/j.enconman.2023.117081.